ALD assisted nanoplasmonic slot waveguide for on-chip enhanced Raman spectroscopy

Ali Raza, Stéphane Clemmen, Pieter Wuytens, Muhammad Muneeb, Michiel Van Daele, Jolien Dendooven, Christophe Detavernier, Andre Skirtach, and Roel Baets

Citation: APL Photonics **3**, 116105 (2018); doi: 10.1063/1.5048266
View online: https://doi.org/10.1063/1.5048266
View Table of Contents: http://aip.scitation.org/toc/app/3/11
Published by the American Institute of Physics

ALD assisted nanoplasmonic slot waveguide for on-chip enhanced Raman spectroscopy

Ali Raza,[1,2,a] Stéphane Clemmen,[1,2,3] Pieter Wuytens,[1,2] Muhammad Muneeb,[1,2] Michiel Van Daele,[4] Jolien Dendooven,[4] Christophe Detavernier,[4] Andre Skirtach,[1,5] and Roel Baets[1,2]
[1]*Center for Nano- and Biophotonics, Ghent University, Ghent 9000, Belgium*
[2]*Photonics Research Group, INTEC Department, Ghent University-imec, Technologiepark-Zwijnaarde, Ghent 9052, Belgium*
[3]*Laboratoire d'Information Quantique, Université Libre de Bruxelles, 1050 Bruxelles, Belgium*
[4]*Department of Solid State Sciences, CoCooN Research Group, Krijgslaan 281/51, Ghent 9000, Belgium*
[5]*Department of Molecular Biotechnology, Ghent University, Ghent 9000, Belgium*

(Received 12 July 2018; accepted 15 September 2018; published online 10 October 2018)

Surface enhanced Raman spectroscopy (SERS) is a widely known sensing technique that uses a plasmonic enhancement to probe analytes in ultra-small volumes. Recently, the integration of plasmonic structures with photonic integrated waveguides promised the full integration of a SERS system on a chip. Unfortunately, the previously reported sensors provide modest overall SERS enhancement resulting in a limited signal to noise ratio. Here, we report a photonic waveguide interfaced SERS sensor that shows an order of magnitude higher pump to Stokes conversion efficiency and lower background than previous realizations. Moreover, the plasmonic structure is fabricated without the use of e-beam lithography but rather using a combination of atomic layer deposition and deep UV photolithography. We investigate numerically the performance of the sensor in terms of Raman conversion efficiency for various design parameters. The experimental results are presented via the acquisition of SERS spectra that show a conversion efficiency of 10^{-9} for a monolayer of 4-nitrothiophenol. To explore the broadband characteristic of our sensor in the therapeutic spectral window, two different pump wavelengths, i.e., 632 and 785 nm, are used. To the best of our knowledge, this is the first ever broadband SERS demonstration of an on-chip Raman sensor. We further study the reproducibility of our SERS sensor, reaching a relative standard deviation of the acquired spectra (RSD) < 5%. https://doi.org/10.1063/1.5048266

I. INTRODUCTION

Recently, the integration of plasmonic structures on photonic platforms has attracted a lot of attention.[1–9] The combination of integrated photonics with plasmonic structures can indeed provide a strong field enhancement over an increased interaction length resulting in a strong light-matter interaction.[10–13] One of the key applications in this context is surface enhanced Raman spectroscopy (SERS). SERS relies on plasmonics enhancement for increasing the electric field strength by many orders of magnitude. Basic SERS substrates are rough gold surfaces that can exhibit large plasmonic enhancement, thanks to tight gaps, but do not offer enough control, homogeneity, and reproducibility of this enhancement. Many SERS substrates have been developed[14–16] providing more reproducible Raman spectra. In parallel to those developments of SERS, Raman spectroscopy enhanced by waveguides was introduced to increase the interaction length between light and analyte while keeping a

[a]Electronic mail: ali.raza@ugent.be

confined beam capable of collecting the spontaneously generated Raman signal.[17] Strip waveguides and slot waveguides have succeeded to earlier demonstration[18–22] due to the combination of high waveguide enhancement and ease of use. Those photonics waveguides still offer relatively lower signal enhancement than what is possible with SERS; however, they are far superior in terms of integration with light sources,[23,24] filters,[25] spectrometers,[26] and detectors,[27] which could be integrated on a single chip as a full Raman system. It is therefore tempting to bring a plasmonic enhancement to the existing photonics integrated circuits (PICs). This has been investigated both theoretically and experimentally using nanoplasmonic antennas.[28–31] A later study made use of microsphere lithography to pattern nanotriangles on a photonic waveguide that gave a better SERS enhancement.[32] However, in the previous reports, a Raman background due to the underlying Si_3N_4 dielectric waveguide[33] was limiting the SNR; therefore, other realizations have been reported, such as combining existing PIC with metallic nanoparticles but at the expense of quantitatively reproducible Raman spectra.[34–36] Here we report the fabrication of metallic slot waveguides that offer both a strong field enhancement due to the highly confined propagating surface plasmon polariton (PSPP) mode and a limited spurious background, thanks to the limited field overlap with the dielectric waveguide. Moreover, the fabrication avoids any use of e-beam lithography and rather relies on the atomic layer deposition (ALD) to create the nanometer scale gaps required for a large plasmonic enhancement. This makes our approach compatible with the back-end CMOS fab. Our sensor relies on SiN photonic circuits fabricated by DUV lithography and reactive ion etching in a CMOS fab. A regular strip waveguide is interfaced to a slot waveguide via a dedicated tapering section.[37] The dielectric waveguide is then conformally coated via atomic layer deposition of Al_2O_3 to reduce the gap of the slot from 150 nm to 34 nm. Subsequently, gold is deposited via sputtering reducing the gap further down to 14.8 nm. The length of the plasmonic structure is defined by a window over which the gold is deposited directly on the Al_2O_3, while the rest of the gold is removed using metal lift-off. Unlike plasmonic nanoantenna, our plasmonic slot waveguide offers micrometer long interaction length and an off-resonant enhancement, hence a broadband Raman conversion efficiency.[38–40] The local enhancement is, therefore, less localized both spectrally and spatially, resulting in an undistorted Raman response and a reduced risk for any field induced damage to the analyte. In this manuscript, we characterize the most important properties of the sensor: SERS enhancement, interaction length, spurious photon background, and signal stability. The sensor is tested using a monolayer of 4-Nitrothiophenol (NTP) whose possible photoreduction to dimercaptoazobenzene (DMAB) is also investigated. In the end, the performance of our reported sensor is compared with other on-chip SERS substrates.

II. DESIGN AND MODELING

The geometry of the sensor is depicted in Fig. 1. The plasmonic sensor is preceded by a low loss 400 μm long Si_3N_4–Al_2O_3 slot waveguide acting as an access waveguide. The length of the plasmonic waveguide is set to 100 μm, far larger than the decay length (15 μm). The fundamental TE mode of the Si_3N_4–Al_2O_3 slot waveguide at a pump wavelength λ_p excites the gap plasmonic mode with a coupling efficiency γ_p. This propagating surface plasmon polariton (PSPP) mode is strongly confined in the gap (g) and interacts with the analyte (NTP) uniformly lying over the gold. The pump beam excites the vibrational modes of the NTP molecules to generate the enhanced Stokes signal that mostly remains coupled to the hybrid plasmonic mode (in both contra- and co-propagating directions). This enhanced pump excitation and subsequent Stokes signal generation can be computed numerically to estimate the Raman conversion efficiency η (see supplementary material). The backward collected signal increases until a certain waveguide length and then saturates due to the decay of the pump light. The saturation length is set by the total waveguide loss α_p. The total Stokes signal P_s normalized by the total guided pump power P_o for the device operating in the aforementioned setup can be defined numerically as

$$\frac{P_s}{P_o} = \zeta = (\gamma_p \gamma_s) \times \eta \times \sigma \times \rho \times \overbrace{\left(\frac{1 - e^{-(\alpha_p + \alpha_s)L_p}}{\alpha_p + \alpha_s}\right)}^{\text{Length factor}}, \tag{1}$$

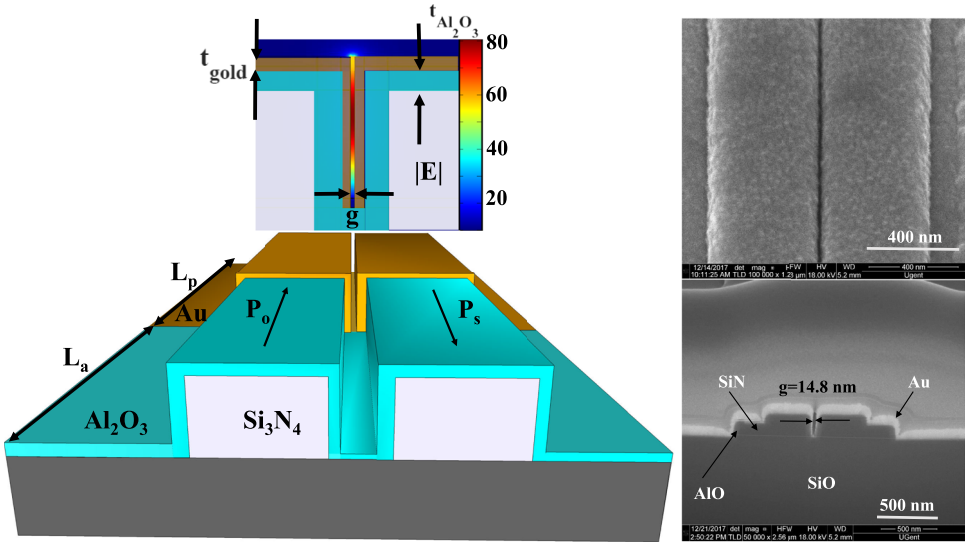

FIG. 1. The schematic of hybrid Si_3N_4–Al_2O_3—gold waveguide. Left top inset shows the propagating plasmon excited using fundamental TE mode of access waveguide. The right insets show the SEM images (top view and cross section of the fabricated device).

where ρ and σ are the molecular density and differential Raman cross section of the analyte. The length factor represents the SERS signal dependence on the plasmonic waveguide length (L_p). To analyze the effect of gold thickness t_{gold} and ALD alumina thickness $t_{Al_2O_3}$, a COMSOL Multiphysics mode solver is used to compute the eigenmodes of the hybrid Si_3N_4 – Al_2O_3 – Au waveguide. We consider a Si_3N_4 slot waveguide with a refractive index of $n_{Si_3N_4} = 1.9$, coated with an Al_2O_3 layer whose refractive index is $n_{Al_2O_3} = 1.6$ and a final thin coating of gold whose complex refractive index is given by the Johnson and Christy model. Our simulation assumes only hybrid-TE excitation (maximum |E| along the surface of the sample) as this mode possesses the highest field confinement into the gap. The electrical field strength |E| is plotted in Fig. 1, showing that the field confinement (≈92% for g = 20 nm) is much stronger than in the case of the Si_3N_4 slot waveguide (≈35% for g = 150 nm). This confinement is expected to strongly reduce the spurious background flux of photons originating from the guiding core of the waveguide (Al_2O_3 and Si_3N_4). The test monolayer of NTP is 1-nm thick and selectively binds to gold. Knowing its refractive index[41] $n_{NTP} = 1.62$ and the Raman resonance of 1339 cm^{-1} ($\nu_s(NO_2)$), we can estimate the conversion efficiency η when the pump wavelength is set to 785 nm and the Stokes wavelength is 877 nm. For a 100 μm long plasmonic waveguide, the ratio $\zeta = P_s/P_o$ of the generated Stokes power over the incoming pump power is plotted in Fig. 2 for a range of thicknesses $t_{Al_2O_3}$ and t_{gold} chosen such that the gap (g) ranges

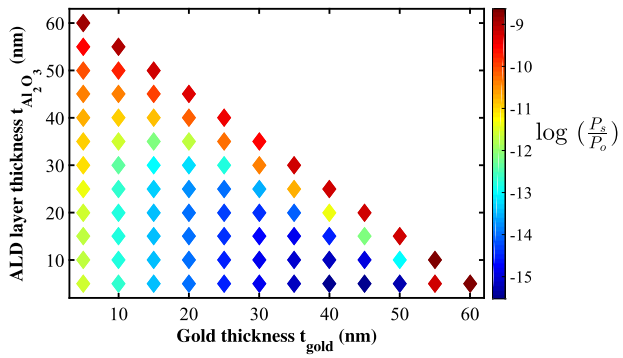

FIG. 2. The dependence of $\zeta = P_s/P_o$ on gold thickness t_{gold} and ALD alumina thickness $t_{Al_2O_3}$ for a 100 μm long plasmonic waveguide. The color bar is plotted in a log scale.

from 150 nm to 10 nm. For simplicity, we keep a constant coupling efficiency, i.e., $\gamma_p = \gamma_s = 5$ dB for all combinations of $t_{Al_2O_3}$ and t_{gold}. The plot shows a nearly constant enhancement for a fixed gap size that is a fixed $t_{Al_2O_3} + t_{gold}$. Of course, this trend does not hold anymore when the gold thickness is so small that the plasmonic effect disappears. For our design, we target a thicker alumina layer (~58 nm) and rather a thin gold layer (~13-16 nm) for two reasons. Indeed, the thickness of Al_2O_3 is experimentally better controlled (thanks to ALD), leading to an easier fabrication. Moreover, a lesser amount of gold also reduces the reflection at the transition between the access and plasmonic waveguide. For $t_{Al_2O_3} = 58$ nm and $t_{gold} = 13$ nm, the plasmonic waveguide losses at the pump (α_p) and Stokes wavelength (α_s) measured using the cut-back method are, respectively, 2.4 and 2.1 dB/μm (see supplementary material). Similarly, the measured γ_p and γ_s are 3.95 and 5.1 dB/facet, respectively. For these values of α_p, α_s, γ_p, and γ_s and a plasmonic waveguide length $L_p = 100$ μm, ζ calculated using the COMSOL Multiphysics mode solver is 1.96×10^{-9}. The single molecule enhancement factor,[42] i.e., SMEF = $|E(\lambda_p)|^2|E(\lambda_s)|^2$ is also calculated by assuming a dipole located in the middle of the gap, i.e., SMEF = 1.5×10^7.

III. EXPERIMENTAL RESULTS AND DISCUSSION

The details about the fabrication can be read in Sec. V. As discussed earlier, the pump wavelength $\lambda_p = 785$ nm is used for all reported results unless it is mentioned explicitly. The description about the experimental conditions and measurement setup is outlined in Sec. V. Raman spectra are measured from both 100 μm long gold coated and 0.6 mm long bare Si_3N_4 slot waveguides, the latter serving as a reference. The results are presented in Fig. 3. Both chips have been processed so that a monolayer of NTP coats the gold nanostructures. Indeed, no NTP peak can be seen from the reference waveguide (free of gold). The spectrum from the plasmonic waveguide shows not only the NTP Raman modes but also a weaker background than the reference waveguide. This is because the pump beam is strongly attenuated in the plasmonic structure and no further Raman background is generated after it. In the absence of gold, light is much less attenuated and a spurious background is generated after the sensor. It is interesting to study the dependence of the SERS signal on the length of the plasmonic waveguide (L_p) and the length of the access waveguide (L_a). In the first set of experiments, the access waveguide

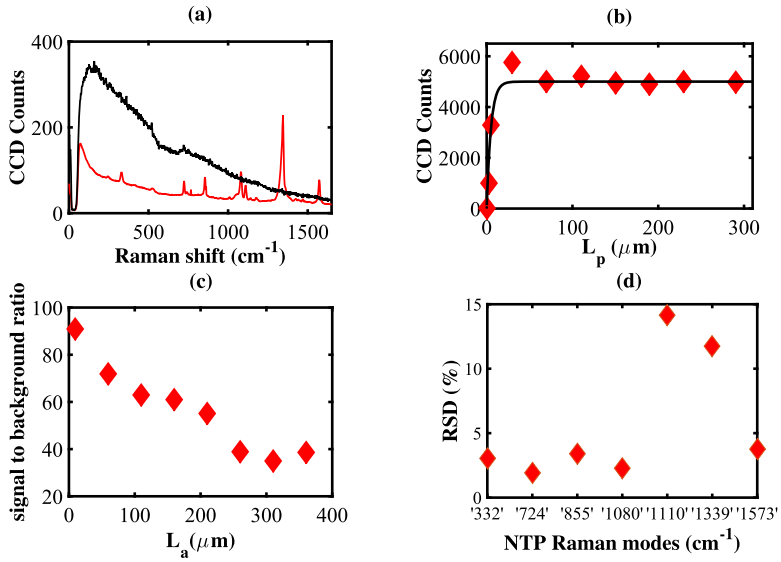

FIG. 3. The measured back-scattered SERS signal of a plasmonic slot waveguide with $t_{Al_2O_3} = 58$ nm and $t_{gold} = 13$ nm. (a) Raman spectrum measured from a functionalized plasmonic waveguide (red curve) and reference waveguide (black curve). (b) SERS signal at 1339 cm^{-1} NTP Raman modes vs the length of plasmonic waveguide (L_p). The black curve represents the length factor fit, from which we extract $\alpha_p = \alpha_s \approx 3.0$ dB/μm. (c) Signal-to-background ratio versus the access waveguide length and (d) the relative standard deviation percentage (RSD%) of the SERS signal measured from 24 different waveguides on three different chips.

length is kept constant, while the plasmonic waveguide length is varied from 0 to 290 μm. As shown in Fig. 3(b), the signal increases with the waveguide length until 15 μm and then saturates due to the decay of the pump light. Fitting the length factor of Eq. (1) gives $\alpha_p = \alpha_s = 3.0 \pm 1.2$ dB/μm, where the large error bar is due to the limited number of points at short waveguide lengths. This value fits well to the α_p and α_s measured using the cut-back method, i.e., 2.4 dB/μm and 2.1 dB/μm, respectively. This interaction length is rather long for a plasmonic structure, and this obviously contributes to the Raman conversion efficiency. It is worth mentioning that α_p depends on the final plasmonic gap (g), i.e., it increases with decreasing plasmonic gap due to the higher modal interaction with gold.[43] In the second set of measurements, the effect of the access waveguide length (L_a) is investigated. As confirmed by Fig. 3(a), the access waveguide does not contribute to the NTP spectrum. However, it does generate a broadband background that can mask the SERS signal of interest if its length is too large.[44] Therefore 8 different access waveguide lengths L_a from 10 to 410 μm with a step size of 50 μm are measured using the same experimental parameters. As shown in Fig. 3(c), the signal to background ratio decreases with increasing access waveguide length. As a third experiment, we explore the spatial reproducibility of the SERS spectra by measuring the relative standard deviation percentage (RSD%) of the SERS signal of all the Raman modes of NTP for 24 different waveguides from three different chips (eight each). Each spectrum is measured using the same pump power, access waveguide length, CCD settings, and integration time. All Raman spectra measured from different waveguides are reported in supplementary material. As shown in Fig. 3(d), all NTP modes except 1080 and 1339 cm^{-1} show high stability with RSD% < 5%. This limited variation is mainly attributed to differences in coupling efficiencies, random gold roughness, and optical alignment inaccuracy. The increased variability at the 1080 and 1339 cm^{-1} modes is attributed to the chemical instability of the NTP exposed to high optical fields and will be discussed hereafter. This SERS signal variation in our plasmonic slot waveguide is comparable to state-of-the-art SERS substrates for free-space excitation at 785 nm pump wavelength.[45,46]

While most plasmonic structures used for SERS rely on a localized surface plasmon resonance, our plasmonic slot waveguide uses a gap propagating surface plasmon polariton (PSPP) that offers broadband and off-resonant enhancement. As a consequence, we expect a signal enhancement that has a reduced dependence on the excitation- and emission wavelength. To demonstrate this broadband nature of the field enhancement, we have taken SERS spectra at two different excitation wavelengths. The reported spectra in Fig. 4(a) are recorded at identical pump power and integration time but for a pump wavelength of 632 nm and 785 nm. The spectrum at shorter wavelength is stronger as compared to the one resulting from 785 nm excitation. However, the spurious background level also increases due to the relatively stronger photoluminescence of gold at shorter wavelength.[47] This result highlights the broadband enhancement of our Raman sensor and the fact that it can be used for any Stokes Raman shift contrasting with the field enhancement in nanoplasmonic antenna where

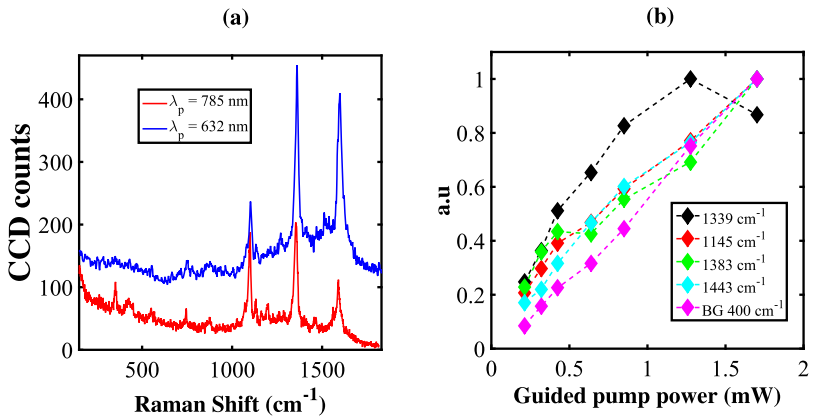

FIG. 4. (a) The back-scattered Raman spectra measured at a pump wavelength of $\lambda_p = 632$ nm (blue curve) and $\lambda_p = 785$ nm (red curve). (b) The photo-induced reduction of 4-NTP into DMAB monitored using integrated counts at 1339, 1145, 1383, and 1443 cm^{-1} vs total guided power. The Si_3N_4 background (BG) is also plotted at 400 cm^{-1}.

the resonance is limited to ≈100 nm. To the best of our knowledge, this is the first broadband SERS demonstration of an on-chip SERS sensor.

Another common limitation of plasmonic structures for Raman spectroscopy is the maximum optical excitation power $P_o^{\max}$ that can be used before degrading the sample/analyte under study. Indeed, this limits the pump power that can be used and therefore the strength of the Raman signal. Due to the relatively low localization of the electric field, our propagating plasmon based sensor is expected to have large $P_o^{\max}$. When exposed to too large intensity, NTP molecules start to photoreduce in a form of dimercaptoazobenzene (DMAB). In order to find $P_o^{\max}$, a series of spectra has been recorded at different pump powers with 1 s integration time each. The photo-degradation of NTP to dimercaptoazobenzene (DMAB) can be monitored using the SERS intensity at 1339 cm^{-1} vs P_O. The power level at which I_{1339} shows nonlinearity against P_O corresponds to the photoreduction of NTP into DMAB. As presented in Fig. 4(b), the 1339 cm^{-1} peak starts to decay after $P_o^{\max}$ = 0.8 mW pump power guided into the access waveguide, while the peaks at 1145 cm^{-1} due to β(CH) and 1383 and 1443 cm^{-1} due to ν(N = N) increase in intensity that shows the gradual conversion of NTP to DMAB. The Si_3N_4 background at 400 cm^{-1} also scales linearly with the pump power confirming no photo-damage to Si_3N_4 at higher powers. A similar observation has been reported before,[48,49] where NTP molecules that bind to a SERS substrate were excited at the pump wavelength of 532 and 632 nm using the free space optics.

Next, we made a comparison between the Raman signal strength obtained through a metal slot waveguide excitation and collection (waveguide excited) versus the excitation and collection through a high NA conventional microscope objective [top-down free space (FS)]. A 2 mW pump power before the objective (Zeiss 100×/0.9 EC Epiplan NEOFLUAR: ∞/0) and 60 s integration time are used for both cases. The results are shown in Fig. 5. First, a reference spectrum is measured through top-down excitation and collection from a position on the sample containing no metal slot waveguide. No NTP peak is seen in the reference spectrum (red curve). Next, a spectrum is recorded from a metal slot waveguide (green curve). The spectrum contains the dominant modes of NTP, i.e., 1110, 1339, and 1573 cm^{-1}. Also, both spectra contain the 520 cm^{-1} Raman detuning of the underlying silicon substrate. Finally, the light is butt coupled to the same metal slot waveguide preceded by 100 μm reference waveguide. The collected Raman spectrum (blue curve) is shown in Fig. 5. The waveguide excited and collected spectrum shows all Raman modes of NTP. The results show that for a fixed pump power before an objective, the Raman signal strength of a metal slot waveguide is approximately 30 times larger as compared to that using a 0.9 NA objective. This is attributed to the long interaction length of the former case. Also, the SNR ($Sig/\sqrt{BG}$) of the former case is approximately 7 times larger than that of the latter case. This comparison is based on the signal counts that correspond to the 1339 cm^{-1} NTP mode.

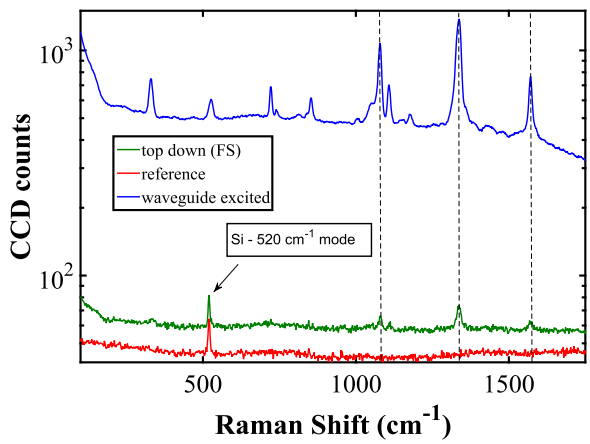

FIG. 5. The Raman spectra measured through excitation and collection from a metal slot waveguide (blue curve) and conventional microscope objective (green curve). All spectra are extracted using the same pump power (2 mW) and integration time (60 s). The black dotted lines show the position of dominant NTP Raman modes.

TABLE I. Comparison of hybrid plasmonic waveguide (HPW) sensor with existing nanophotonic SERS substrates, i.e., nanobowties (NBs) and nanotriangles (NTs).

Structures	$\zeta = P_s/P_o$	N_{mol}	Fabrication technique	Resonance FWHM (nm)
NB[31,44]	$\approx 10^{-12}$	$\approx 0.5 \times 10^7$	e-beam	≤ 100
NT[32]	$\approx 10^{-10}$	$\approx 1.5 \times 10^7$	Nanosphere litho.	≤ 250
HPW	$(1 \pm 0.057)\ 10^{-9}$	$\approx 8.2 \times 10^7$	ALD + photolitho.	Non-resonant

Finally, we compare our hybrid plasmonic waveguide based sensor (HPW) with previously published on-chip surface enhanced Raman sensors, i.e., nanobowties (NBs)[31,44] fabricated using e-beam lithography and nanotriangles (NTs)[32] fabricated using nanosphere lithography. The comparison is presented in Table I in terms of measured Raman conversion efficiency ($\zeta = P_s/P_o$), number of molecules (N_{mol}) excited, resonance behavior, and fabrication technique. The experimental value of ζ for our nanoplasmonic sensor that is extracted for the 1339 cm^{-1} mode of NTP is $(1 \pm 0.057) \times 10^{-9}$. This is 3 orders of magnitude higher than that of nanobowties and an order of magnitude higher than that of nanotriangles. The total number of molecules excited (N_{mol}) in each case is calculated using $A_g \times \rho_g$ where A_g is the gold surface area and $\rho_g = 4.4 \times 10^6$ molecules/μm^2 (Ref. 50) is the density of NTP molecules on a gold surface. Another advantage of the reported SERS substrate over others is the ease of fabrication that consists of ALD assisted DUV photolithography, which enables mass scale manufacturing. Next, the broadband nature of SERS enhancement is compared with the other two devices. NB and NT are highly resonant, i.e., FWHM of resonant enhancement ≤ 100 nm for nanobowties and ≤ 250 nm for nanotriangles. Our sensor offers a non-resonant enhancement, making the SERS enhancement independent of excited and scattered wavelengths. In the end, we numerically compare the signal strength offered by a hybrid plasmonic waveguide (HPW) based sensor with a standard silicon nitride strip and slot (gap = 150 nm) waveguide[19,39] fabricated using DUV photolithography. Two different cases, i.e., a monolayer of NTP and a bulk Isopropyl Alcohol (IPA) cladding, are considered. The results are presented in Table II (italic). In the case of an NTP monolayer, for the sake of comparison, we assume the same NTP Raman cross section ($\sigma = 1.8 \times 10^{-29}$ cm^2/sr) and surface density ($\rho = 4.4 \times 10^6$ molecules/μm^2) for both sensors. However, this is rather an artificial assumption because ρ of a given molecule strongly depends on the surface of the substrate as well as the binding technique. But it serves the purpose of comparing different sensors. For an NTP monolayer, 15 μm long HPW exhibits approximately 14 and 20 times stronger signal as compared to a 4 cm long silicon nitride slot and a 5 cm long strip waveguide. Here, we have considered the coupling loss from an access waveguide to a plasmonic waveguide, i.e., γ_p and γ_s are 3.95 and 5.1 dB/facet, respectively. Similarly, for a bulk analyte, ζ is computed assuming a 5 μm thick IPA as a top cladding ($n_{IPA} = 1.37$, $\lambda_p = 785$ nm, $\lambda_s = 840$ nm, $\sigma = 8.0 \times 10^{-31}$ cm^2/sr, and $\rho = 7.87 \times 10^{21}$ molecules/cm^3).[39] In spite of the high field enhancement offered by a HPW, ζ for the silicon nitride slot waveguide is still approximately 3 times larger than for a HPW. This is attributed to a long interaction length and large modal overlap with the analyte. Note that in this comparison, the spurious Raman background generated from the waveguide core[33] is not taken into account, which is indeed a major limiting factor in achieving high SNR in the dielectric waveguide based Raman sensors.

TABLE II. Comparison of a hybrid plasmonic waveguide (HPW) sensor with a Si_3N_4 strip and slot waveguide for an NTP monolayer (bold) and for a bulk isopropyl alcohol cladding (italic).

Structures	$\zeta = P_s/P_o$	Effective length
Metal slot	$\mathbf{1.0 \times 10^{-9}}$ $\mathit{1.2 \times 10^{-10}}$	$\approx 15\ \mu$m
Si_3N_4 slot	$\mathbf{7.0 \times 10^{-11}}$ $\mathit{3.4 \times 10^{-10}}$	≈ 4 cm
Si_3N_4 strip	$\mathbf{5.0 \times 10^{-11}}$ $\mathit{1.1 \times 10^{-10}}$	≈ 5 cm

IV. CONCLUSION

In conclusion, we have reported a SERS sensor suitable for on-chip integrated Raman spectroscopy, fabricated using ALD assisted DUV lithography and therefore compatible with the back-end CMOS fabrication. We have reported both the experimental and numerical characterization of our sensor demonstrating capabilities that have so far been difficult to combine in a single sensor: (1) a large Raman conversion efficiency ($\approx 1 \times 10^{-9}$), thanks to simultaneous long interaction length, high confinement, and plasmonic enhancement (SMEF = 1.5×10^{7}), (2) a low background due to the reduced overlap of the field with the core of the waveguide, (3) a good reproducibility of the Raman spectra (RSD < 5%) across different chips, thanks to the nanometer fabrication accuracy provided by atomic layer deposition, (4) a good tolerance to rather large input power due to a moderate local field enhancement, and (5) a broadband enhancement, thanks to the use of propagating plasmons rather than localized plasmon (nanoantennae). All these features make this kind of sensor ideal for the future integration with lasers, spectrometers, spectral filters, and detectors that will constitute a fully integrated Raman spectrometer chip. Given the compactness of our plasmonic sensor and the other elements, it is easy to foresee a chip capable of containing dozens or hundreds of sensors for performing multiplexed Raman sensing. Such an application is of great importance in biology,[51,52] especially the study of proteins accessible to small gaps.[53] Also, our choice of a monolayer as an analyte supports many bio-applications from clinical diagnostics, proteomics, genomics, and biomaterials to tissue engineering.[54–57] Moreover, our fabrication method may also open the way to other plasmonic-enabled applications that remained to date confined to the laboratory because of the need for e-beam lithography. This is the case for fast optical switches,[58,59] efficient frequency converters,[60] or optical nanoscopy.[61]

V. METHODS

A. Fabrication

Si_3N_4 slot waveguides used for our experiments are fabricated on a 200 mm silicon wafer containing a stack of 2.3 ± 0.1 μm thick high-density plasma enhanced chemical vapor deposition (PECVD) silicon oxide SiO_2 and 220 nm thick PECVD Si_3N_4.[62] The structures were patterned with 193 nm optical lithography and subsequently etched by fluorine based inductive coupled plasma-reactive ion-etch process to attain the final structure. The resulting average slot width is 150 nm. The waveguide topology is depicted in Fig. 6. Then, the structure is conformally coated with 58 nm of Al_2O_3 using atomic layer deposition (ALD). Due to a significant modal overlap with Al_2O_3, as shown in Fig. 6(b), the amount of Raman background from the Al_2O_3 layer is very low. In order to compare the Raman background generated by bulk Al_2O_3 and PECVD Si_3N_4, top-down Raman measurements are taken on two samples, i.e., 100 nm Al_2O_3/1 mm CaF_2 and 220 nm Si_3N_4/1 mm CaF_2. Both spectra are recorded using 10 mW pump power and 30 s integration time. The Raman spectra after thickness normalization are shown in Fig. 6(c). The result shows that Al_2O_3 exhibits minimal Raman background as compared to PECVD Si_3N_4. The ALD deposition is performed in a home built ALD setup that has a base pressure of 10^{-6} mbar. Deposition of the Al_2O_3 layer is performed using a thermal ALD process[63] at a substrate temperature of 120 °C using trimethylaluminum and water pulses of 5 s at 5×10^{-3} mbar. After the Al_2O_3 deposition, AZ 5214 resist is spin coated over the chip using 3500 RPM and 40 s spinning time. This is followed by an 11 s DUV exposure, 3 min post-bake at 120 °C, and a 50 s DUV flood exposure (for image reversal). After the DUV exposure, the development was performed in a solution containing AZ400:DI-water (3:1). A short O_2 plasma (PVA-TEPLA GIGAbatch 310 m, 6000 SCCM O2, 600 W, 750 mTorr) was performed to remove the residual resist. A thin 1-2 nm of Ti followed by a 13-15 nm of gold along the side wall is deposited using the Au-sputtering. Finally, a 100 μm gold waveguide is defined using the metal lift. In order to characterize the performance of our device, the sensor is functionalized with a monolayer of 4-nitrophenol that selectively binds to the gold. It is worth mentioning that in the future, the ALD coating step may become obsolete because of the use of extreme-UV sources for integrated photonics, as is currently happening in the nanoelectronics industry.

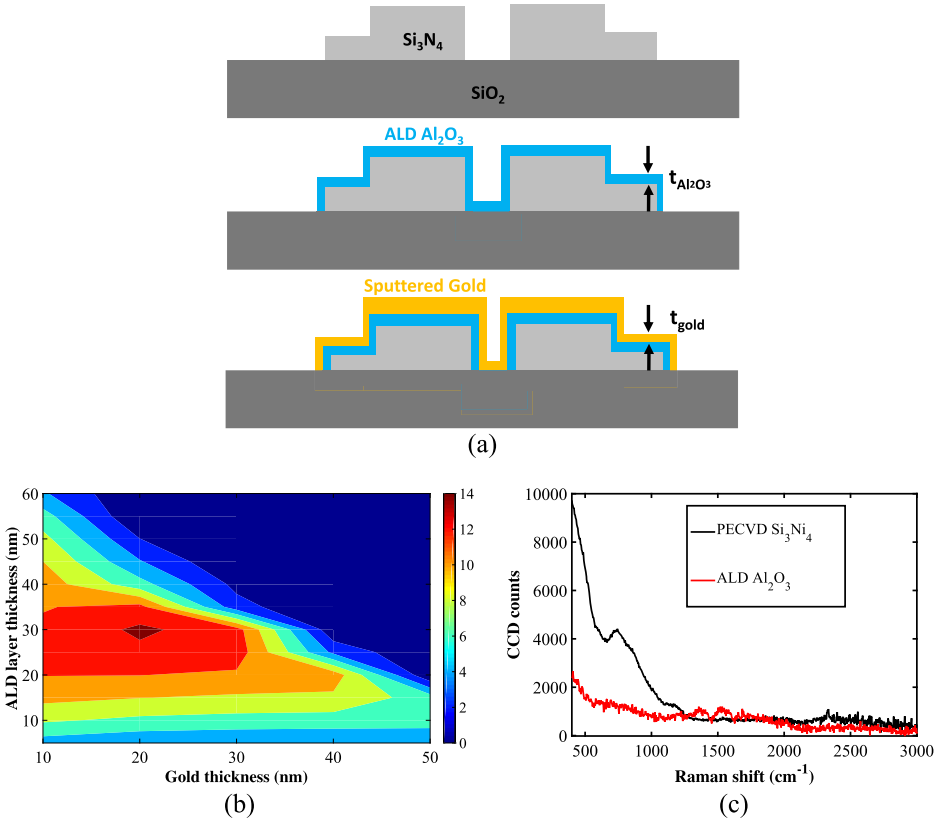

FIG. 6. The fabrication details of the device. (a) The process flow of the device showing the three main steps. (b) The simulated modal confinement (%) in the ALD Al_2O_3 layer. (c) Comparison of Raman background from Si_3N_4 and ALD Al_2O_3 deposited on CaF_2 substrates and measured using a top-down excitation by a commercial Raman microscope.

B. 4-nitrophenol (NTP)—Gold binding

We use a standard binding recipe, e.g., chemisorption of thiols from an ethanolic solution,[64] to get a self-assembled monolayer of NTP. The procedure is as follows: the chips are cleaned thoroughly by first rinsing with acetone and isopropyl alcohol in an ultrasonic bath, followed by a 5 min exposure to an O_2 plasma. The chips are then immersed overnight into a beaker containing 1 mM NTP solution in ethanol. This is followed by a deep cleaning using pure ethanol and N_2 dry clean. As a result, a uniform monolayer of NTP is formed on top of the gold through gold-sulfur bond. Note that an overnight soaking to form an NTP monolayer is an overkill and this procedure can be accelerated (<1 h) by optimizing the thiol-ethanolic solution.[41,65] Similarly, the accessibility of an analyte to a narrow slot can also be enhanced using wetting techniques.[66]

C. Measurement setup

A commercial confocal Raman microscope (WITEC Alpha300R+) is used for coupling the light in and out of the chip, which is positioned vertically and end-fire coupled, as shown in Fig. 7. A 785 nm excitation diode laser (Toptica XTRA II) is used for excitation. The polarization of the excitation beam is set to the TE mode of the waveguide. A laser power of 1 mW measured before the entrance facet of a Zeiss 100×/0.9 EC Epiplan NEOFLUAR: ∞/0 objective is used. The scattered signal is collected in back reflection using the same objective and imaged on a 100 μm multimode fiber. This fiber functions as a confocal pinhole and entrance slit of the spectrometer. The spectrometer uses a 600 lines/mm grating to disperse the light onto a −73 °C cooled CCD camera (ANDOR iDus 401 BR-DD). In addition to that, an integrated sphere connected to a ThorLabs powermeter is used at the waveguide end facet to monitor the transmission. The objective and chip are aligned with

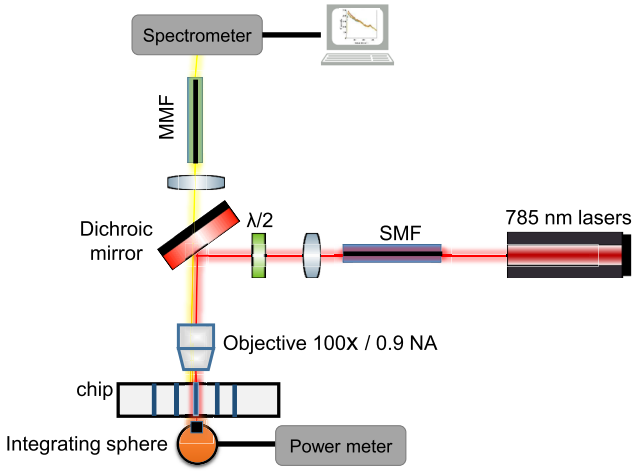

FIG. 7. A schematic of an optical setup use to measure the Raman spectrum.

100 nm accuracy based on a maximum intensity of the waveguide Raman spectrum. Simultaneously, maximum light scattering along the waveguide is observed from a camera imaging the top surface of the chip.

SUPPLEMENTARY MATERIAL

Supplementary material consists of three different sections. The first section describes the derivation of η and ζ, presented in Eq. (1). The second section consists of plasmonic waveguide loss measurements. In the last section, the NTP Raman spectra measured from 24 different waveguides are reported.

ACKNOWLEDGMENTS

The authors acknowledge Professor Pol Van Dorpe (imec) and Professor Nicolas Le Thomas (UGent) for useful discussion. We also acknowledge Liesbet Van Landschoot for taking the SEM images.

This research was funded by the ERC Grant InSpectra and FWO Belgium. Stéphane Clemmen thanks the F.R.S-FNRS for financial support. We also acknowledge the support of BOF (UGent, Belgium).

[1] A. L. Pyayt, B. Wiley, Y. Xia, A. Chen, and L. Dalton, "Integration of photonic and silver nanowire plasmonic waveguides," Nat. Nanotechnol. **3**, 660–665 (2008).
[2] A. Melikyan, L. Alloatti, A. Muslija, D. Hillerkuss, P. C. Schindler, J. Li, R. Palmer, D. Korn, S. Muehlbrandt, D. Van Thourhout, B. Chen, R. Dinu, M. Sommer, C. Koos, M. Kohl, W. Freude, and J. Leuthold, "High-speed plasmonic phase modulators," Nat. Photonics **8**, 229–233 (2014).
[3] A. Espinosa-Soria, A. Griol, and A. Martínez, "Experimental measurement of plasmonic nanostructures embedded in silicon waveguide gaps," Opt. Express **24**, 9592–9601 (2016).
[4] B. Chen, R. Bruck, D. Traviss, A. Z. Khokhar, S. Reynolds, D. J. Thomson, G. Z. Mashanovich, G. T. Reed, and O. L. Muskens, "Hybrid photon–plasmon coupling and ultrafast control of nanoantennas on a silicon photonic chip," Nano Lett. **18**, 610–617 (2018).
[5] F. Peyskens, A. Z. Subramanian, P. Neutens, A. Dhakal, P. V. Dorpe, N. L. Thomas, and R. Baets, "Bright and dark plasmon resonances of nanoplasmonic antennas evanescently coupled with a silicon nitride waveguide," Opt. Express **23**, 3088–3101 (2015).
[6] M. Chamanzar and A. Adibi, "Hybrid nanoplasmonic-photonic resonators for efficient coupling of light to single plasmonic nanoresonators," Opt. Express **19**, 22292–22304 (2011).
[7] M. Darvishzadeh-Varcheie, C. Guclu, R. Ragan, O. Boyraz, and F. Capolino, "Electric field enhancement with plasmonic colloidal nanoantennas excited by a silicon nitride waveguide," Opt. Express **24**, 28337–28352 (2016).
[8] Y. Luo, M. Chamanzar, A. Apuzzo, R. Salas-Montiel, K. N. Nguyen, S. Blaize, and A. Adibi, "On-chip hybrid photonic–plasmonic light concentrator for nanofocusing in an integrated silicon photonics platform," Nano Lett. **15**, 849–856 (2015).
[9] X. He, L. Yang, and T. Yang, "Optical nanofocusing by tapering coupled photonic-plasmonic waveguides," Opt. Express **19**, 12865–12872 (2011).

[10] Y.-F. Xiao, Y.-C. Liu, B.-B. Li, Y.-L. Chen, Y. Li, and Q. Gong, "Strongly enhanced light-matter interaction in a hybrid photonic-plasmonic resonator," Phys. Rev. A **85**, 031805 (2012).
[11] P. Vasa and C. Lienau, "Strong light–matter interaction in quantum emitter/metal hybrid nanostructures," ACS Photonics **5**, 2–23 (2018).
[12] J. A. Schuller, E. S. Barnard, W. Cai, Y. C. Jun, J. S. White, and M. L. Brongersma, "Plasmonics for extreme light concentration and manipulation," Nat. Mater. **9**, 193–204 (2010).
[13] S. Tanwar, K. K. Haldar, and T. Sen, "DNA origami directed Au nanostar dimers for single-molecule surface-enhanced Raman scattering," J. Am. Chem. Soc. **139**, 17639–17648 (2017).
[14] A. X. Wang and X. Kong, "Review of recent progress of plasmonic materials and nano-structures for surface-enhanced Raman scattering," Materials **8**, 3024–3052 (2015).
[15] B.-S. Lee, D.-Z. Lin, and T.-J. Yen, "A low-cost, highly-stable surface enhanced Raman scattering substrate by Si nanowire arrays decorated with Au nanoparticles and Au backplate," Sci. Rep. **7**, 4604 (2017).
[16] P. C. Wuytens, A. Z. Subramanian, W. H. De Vos, A. G. Skirtach, and R. Baets, "Gold nanodome-patterned microchips for intracellular surface-enhanced Raman spectroscopy," Analyst **140**, 8080–8087 (2015).
[17] S. O. Konorov, C. J. Addison, H. G. Schulze, R. F. B. Turner, and M. W. Blades, "Hollow-core photonic crystal fiber-optic probes for Raman spectroscopy," Opt. Lett. **31**, 1911–1913 (2006).
[18] A. Dhakal, A. Z. Subramanian, P. Wuytens, F. Peyskens, N. L. Thomas, and R. Baets, "Evanescent excitation and collection of spontaneous Raman spectra using silicon nitride nanophotonic waveguides," Opt. Lett. **39**, 4025–4028 (2014).
[19] A. Dhakal, P. C. Wuytens, F. Peyskens, K. Jans, N. L. Thomas, and R. Baets, "Nanophotonic waveguide enhanced Raman spectroscopy of biological submonolayers," ACS Photonics **3**, 2141–2149 (2016).
[20] S. A. Holmstrom, T. H. Stievater, D. A. Kozak, M. W. Pruessner, N. Tyndall, W. S. Rabinovich, R. A. McGill, and J. B. Khurgin, "Trace gas Raman spectroscopy using functionalized waveguides," Optica **3**, 891–896 (2016).
[21] C. C. Evans, C. Liu, and J. Suntivich, "TiO_2 nanophotonic sensors for efficient integrated evanescent Raman spectroscopy," ACS Photonics **3**, 1662–1669 (2016).
[22] Z. Wang, M. N. Zervas, P. N. Bartlett, and J. S. Wilkinson, "Surface and waveguide collection of Raman emission in waveguide-enhanced Raman spectroscopy," Opt. Lett. **41**, 4146–4149 (2016).
[23] Z. Zhou, B. Yin, and J. Michel, "On-chip light sources for silicon photonics," Light: Sci. Appl. **4**, e358 (2015).
[24] E. P. Haglund, S. Kumari, P. Westbergh, J. S. Gustavsson, G. Roelkens, R. Baets, and A. Larsson, "Silicon-integrated short-wavelength hybrid-cavity VCSEL," Opt. Express **23**, 33634–33640 (2015).
[25] Z. Zou, L. Zhou, X. Li, and J. Chen, "60-nm-thick basic photonic components and Bragg gratings on the silicon-on-insulator platform," Opt. Express **23**, 20784–20795 (2015).
[26] X. Nie, E. Ryckeboer, G. Roelkens, and R. Baets, "CMOS-compatible broadband co-propagative stationary Fourier transform spectrometer integrated on a silicon nitride photonics platform," Opt. Express **25**, A409–A418 (2017).
[27] J. Michel, J. Liu, and L. C. Kimerling, "High-performance Ge-on-Si photodetectors," Nat. Photonics **4**, 527 (2010).
[28] F. Tang, P.-M. Adam, and S. Boutami, "Theoretical investigation of SERS nanosensors based on hybrid waveguides made of metallic slots and dielectric strips," Opt. Express **24**, 21244–21255 (2016).
[29] A. Raza, F. Peyskens, S. Clemmen, and R. Baets, "Towards single antenna on-chip surface enhanced Raman spectroscopy: Arch dipole antenna," in 7th International Conference on Metamaterials, Photonic Cyrstals and Plasmonics (META'16), 2016.
[30] G. Singh, R. Bi, U. S. Dinish, and M. Olivo, "Generating localized plasmonic fields on an integrated photonic platform using tapered couplers for biosensing applications," Sci. Rep. **7**, 15587 (2017).
[31] F. Peyskens, A. Dhakal, P. Van Dorpe, N. Le Thomas, and R. Baets, "Surface enhanced Raman spectroscopy using a single mode nanophotonic-plasmonic platform," ACS Photonics **3**, 102–108 (2016).
[32] P. C. Wuytens, A. G. Skirtach, and R. Baets, "On-chip surface-enhanced Raman spectroscopy using nanosphere-lithography patterned antennas on silicon nitride waveguides," Opt. Express **25**, 12926–12934 (2017).
[33] N. L. Thomas, A. Dhakal, A. Raza, F. Peyskens, and R. Baets, "Impact of fundamental thermodynamic fluctuations on light propagating in photonic waveguides made of amorphous materials," Optica **5**, 328–336 (2018).
[34] P. Measor, L. Seballos, D. Yin, J. Z. Zhang, E. J. Lunt, A. R. Hawkins, and H. Schmidt, "On-chip surface-enhanced Raman scattering detection using integrated liquid-core waveguides," Appl. Phys. Lett. **90**, 211107 (2007).
[35] L. Kong, C. Lee, C. M. Earhart, B. Cordovez, and J. W. Chan, "A nanotweezer system for evanescent wave excited surface enhanced Raman spectroscopy (SERS) of single nanoparticles," Opt. Express **23**, 6793–6802 (2015).
[36] S. Lin, W. Zhu, Y. Jin, and K. B. Crozier, "Surface-enhanced Raman scattering with Ag nanoparticles optically trapped by a photonic crystal cavity," Nano Lett. **13**, 559–563 (2013).
[37] V. R. Almeida, R. R. Panepucci, and M. Lipson, "Nanotaper for compact mode conversion," Opt. Lett. **28**, 1302–1304 (2003).
[38] Y. C. Jun, R. D. Kekatpure, J. S. White, and M. L. Brongersma, "Nonresonant enhancement of spontaneous emission in metal-dielectric-metal plasmon waveguide structures," Phys. Rev. B **78**, 153111 (2008).
[39] A. Dhakal, A. Raza, F. Peyskens, A. Z. Subramanian, S. Clemmen, N. L. Thomas, and R. Baets, "Efficiency of evanescent excitation and collection of spontaneous Raman scattering near high index contrast channel waveguides," Opt. Express **23**, 27391–27404 (2015).
[40] H. M. Wong, M. K. Dezfouli, L. Sun, S. Hughes, and A. S. Helmy, "Nanoscale plasmonic slot waveguides for enhanced Raman spectroscopy," Phys. Rev. B **98**, 085124 (2018).
[41] A. Jakubowicz, H. Jia, R. M. Wallace, and B. E. Gnade, "Adsorption kinetics of p-nitrobenzenethiol self-assembled monolayers on a gold surface," Langmuir **21**, 950–955 (2005).
[42] F. J. García-Vidal and J. Pendry, "Collective theory for surface enhanced Raman scattering," Phys. Rev. Lett. **77**, 1163 (1996).
[43] L. Chen, J. Shakya, and M. Lipson, "Subwavelength confinement in an integrated metal slot waveguide on silicon," Opt. Lett. **31**, 2133–2135 (2006).

[44] F. Peyskens, P. Wuytens, A. Raza, P. Van Dorpe, and R. Baets, "Waveguide excitation and collection of surface-enhanced Raman scattering from a single plasmonic antenna," Nanophotonics **7**, 1299 (2018).
[45] J. Li, C. Chen, H. Jans, X. Xu, N. Verellen, I. Vos, Y. Okumura, V. V. Moshchalkov, L. Lagae, and P. Van Dorpe, "300 mm wafer-level, ultra-dense arrays of Au-capped nanopillars with sub-10 nm gaps as reliable SERS substrates," Nanoscale **6**, 12391–12396 (2014).
[46] H.-Y. Wu, C. J. Choi, and B. T. Cunningham, "Plasmonic nanogap-enhanced Raman scattering using a resonant nanodome array," Small **8**, 2878–2885 (2012).
[47] C. Chen, J. A. Hutchison, P. V. Dorpe, R. Kox, I. D. Vlaminck, H. Uji-i, J. Hofkens, L. Lagae, G. Maes, and G. Borghs, "Focusing plasmons in nanoslits for surface-enhanced Raman scattering," Small **5**, 2876–2882 (2009).
[48] M. Tabatabaei, A. Sangar, N. Kazemi-Zanjani, P. Torchio, A. Merlen, and F. Lagugne-Labarthet, "Optical properties of silver and gold tetrahedral nanopyramid arrays prepared by nanosphere lithography," J. Phys. Chem. C **117**, 14778–14786 (2013).
[49] L. Kang, P. Xu, B. Zhang, H. Tsai, X. Han, and H.-L. Wang, "Laser wavelength- and power-dependent plasmon-driven chemical reactions monitored using single particle surface enhanced Raman spectroscopy," Chem. Commun. **49**, 3389–3391 (2013).
[50] L. Baia, M. Baia, J. Popp, and S. Astilean, "Gold films deposited over regular arrays of polystyrene nanospheres as highly effective SERS substrates from visible to NIR," J. Phys. Chem. B **110**, 23982–23986 (2006).
[51] H. J. Butler, L. Ashton, B. Bird, G. Cinque, K. Curtis, J. Dorney, K. Esmonde-White, N. J. Fullwood, B. Gardner, P. L. Martin-Hirsch *et al.*, "Using Raman spectroscopy to characterize biological materials," Nat. Protoc. **11**, 664 (2016).
[52] L. Li, C. Liu, X. Cao, L. Tan, and W. Lu, "Multiplexing determination of cancer-associated biomarkers by surface-enhanced Raman scattering using ordered gold nanohoneycomb arrays," Bioanalysis **9**, 1561–1572 (2017).
[53] L. Bayne, R. V. Ulijn, and P. J. Halling, "Effect of pore size on the performance of immobilised enzymes," Chem. Soc. Rev. **42**, 9000–9010 (2013).
[54] R. B. Gennis, *Biomembranes: Molecular Structure and Function* (Springer Science & Business Media, 2013).
[55] E. Southern, K. Mir, and M. Shchepinov, "Molecular interactions on microarrays," Nat. Genet. **21**, 5 (1999).
[56] P. C. Wuytens, H. Demol, N. Turk, K. Gevaert, A. G. Skirtach, M. Lamkanfi, and R. Baets, "Gold nanodome SERS platform for label-free detection of protease activity," Faraday Discuss. **205**, 345–361 (2017).
[57] B. Lu, M. R. Smyth, and R. O'Kennedy, "Tutorial review. Oriented immobilization of antibodies and its applications in immunoassays and immunosensors," Analyst **121**, 29R–32R (1996).
[58] J. A. Dionne, K. Diest, L. A. Sweatlock, and H. A. Atwater, "Plasmostor: A metaloxidesi field effect plasmonic modulator," Nano Lett. **9**, 897–902 (2009).
[59] C. Haffner, D. Chelladurai, Y. Fedoryshyn, A. Josten, B. Baeuerle, W. Heni, T. Watanabe, T. Cui, B. Cheng, S. Saha, D. L. Elder, L. R. Dalton, A. Boltasseva, V. M. Shalaev, N. Kinsey, and J. Leuthold, "Low-loss plasmon-assisted electro-optic modulator," Nature **556**, 483–486 (2018).
[60] R. B. Davidson, A. Yanchenko, J. I. Ziegler, S. M. Avanesyan, B. J. Lawrie, and R. F. Haglund, "Ultrafast plasmonic control of second harmonic generation," ACS Photonics **3**, 1477–1481 (2016).
[61] F. Balzarotti and F. D. Stefani, "Plasmonics meets far-field optical nanoscopy," ACS Nano **6**, 4580–4584 (2012).
[62] A. Z. Subramanian, P. Neutens, A. Dhakal, R. Jansen, T. Claes, X. Rottenberg, F. Peyskens, S. Selvaraja, P. Helin, B. D. Bois, K. Leyssens, S. Severi, P. Deshpande, R. Baets, and P. V. Dorpe, "Low-loss singlemode PECVD silicon nitride photonic wire waveguides for 532–900 nm wavelength window fabricated within a CMOS pilot line," IEEE Photonics J. **5**, 2202809 (2013).
[63] E. Levrau, K. Van de Kerckhove, K. Devloo-Casier, S. Pulinthanathu Sree, J. A. Martens, C. Detavernier, and J. Dendooven, "*In situ* IR spectroscopic investigation of alumina ALD on porous silica films: Thermal versus plasma-enhanced ALD," J. Phys. Chem. C **118**, 29854–29859 (2014).
[64] J. C. Love, L. A. Estroff, J. K. Kriebel, R. G. Nuzzo, and G. M. Whitesides, "Self-assembled monolayers of thiolates on metals as a form of nanotechnology," Chem. Rev. **105**, 1103–1170 (2005).
[65] S. Asiaei, P. Nieva, and M. M. Vijayan, "Fast kinetics of thiolic self-assembled monolayer adsorption on gold: Modeling and confirmation by protein binding," J. Phys. Chem. B **118**, 13697–13703 (2014).
[66] C. Chen, X. Xu, Y. Li, H. Jans, P. Neutens, S. Kerman, G. Vereecke, F. Holsteyns, G. Maes, L. Lagae, T. Stakenborg, and P. van Dorpe, "Full wetting of plasmonic nanopores through two-component droplets," Chem. Sci. **6**, 6564–6571 (2015).